Foam-Embedded Soft Robotic Joint With Inverse Kinematic Modeling by Iterative Self-Improving Learning

Anlun Huang ⬤, Yongxi Cao ⬤, Jiajie Guo ⬤, Zhonggui Fang ⬤, Yinyin Su ⬤, Sicong Liu ⬤, *Member, IEEE*,
Juan Yi ⬤, *Member, IEEE*, Hongqiang Wang ⬤, *Member, IEEE*, Jian S. Dai ⬤, *Fellow, IEEE*,
and Zheng Wang ⬤, *Senior Member, IEEE*

Abstract—**Soft robotic arms have gained significant attention owing to their flexibility and adaptability. Nonetheless, the instability due to their high-elasticity structure further leads to the difficulty of precise kinematic modeling and control. This letter introduces a novel solution employing foam-embedded joint design (Fe-Joint), effectively mitigating oscillations and enhancing motion stability. This innovation is integrated into the new continuum soft robotic arm (Fe-Arm). Through iterative design optimization, the Fe-Arm attains superior mechanical performance and control capabilities, enabling a settling state in 0.4 seconds post external force. Enabled by the quasi-static behavior of Fe-Arm, we propose a long short-term memory network (LSTM) based iterative self-improving learning strategy (ISL) for end-to-end inverse kinematics modeling, tailored to Fe-Arm's mechanical traits, enhancing modeling performance with limited data. Investigating key control parameters, we achieve target trajectory modeling errors within 9% of the workspace radius. The generalization potential of the ISL method is demonstrated using the pentagonal trajectory and on a different Fe-Arm configuration.**

I. INTRODUCTION

SOFT robotic arms have emerged as a prominent research area in the field of soft robotics, driven by their inherent characteristics of safety, lightweight construction, and compliance [1]. These attributes position them as promising solutions for applications in diverse unstructured environments. Recent studies have reported diverse actuation designs, including pneumatic systems, cable-driven mechanisms, and electroactive polymers [2]. Continuum soft robotic arm structures typically feature three soft actuators connected in parallel, forming a triangular configuration in cross-section [3]. These innovative designs allow soft robotic arms to exhibit distinctive morphologies that deviate from traditional rigid-body counterparts, opening up possibilities for novel tasks and enhanced functionalities [4].

Soft robotic arms employing these actuation methods and structure designs have demonstrated promising motion performance when coupled with carefully designed position or dynamics controllers. However, they often face challenges stemming from undesired oscillations in dynamic scenarios. For instance, experimental results from the FESTO Bionic Handling Assistant (BHA) indicate that when subjected to external forces, the robotic arm undergoes under-damped oscillations lasting approximately three seconds before reaching a stable state [5]. Similarly, the multi-segment manipulator powered by fluidic elastomer actuators also experiences an oscillation period of roughly 10 seconds [6]. This phenomenon significantly limits the potential applications of soft robotic arms. The drawbacks associated with undesired oscillation encompass various aspects, including (a) the inability to sustain substantial external loads, (b) diminished image perception when cameras are integrated as part of the end-effector, and (c) the impracticality of implementing high-frequency feedback dynamic controllers. This problem is not due to immature fabrication or poor controller design, but a result of the high inherent compliance of the actuator material. Soft robotic arms, typically composed of stacked soft actuators or joints, possess high elasticity, exacerbating the amplification of oscillations within the system.

Research on the mechanical performance of soft robotic arms mainly focuses on increasing stiffness and load capacity. A
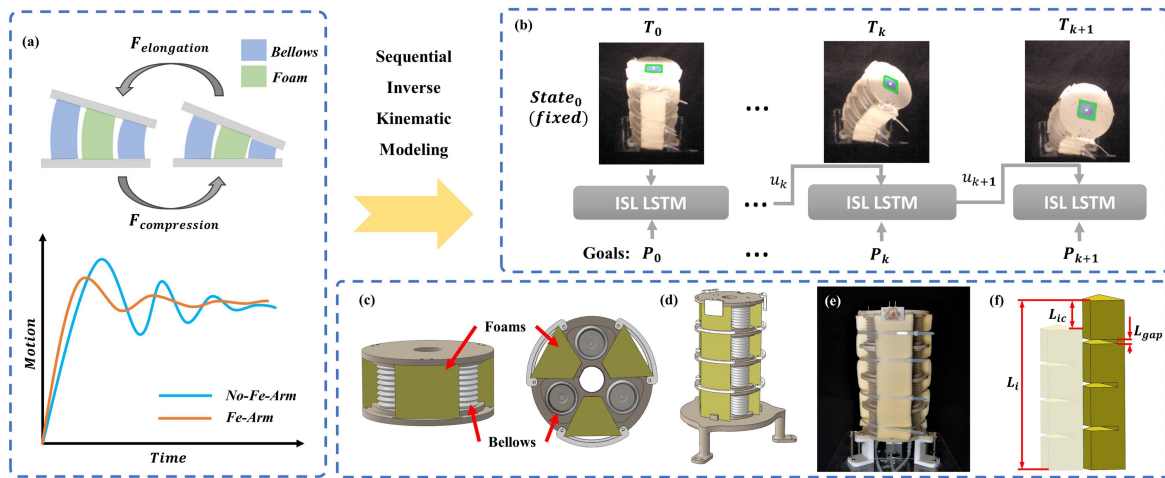
Fig. 1. Concept of (a) the foam-embedded soft robotic joint for mitigating oscillations, and the resultant quasi-static behavior enables the control by sequential inverse kinematics (IK) model, which can be obtained by LSTM-based methods. (b) Overview of the LSTM-based Iterative Self-Improving (ISL) IK model. (c) The Fe-Joint design. (d) The Fe-Arm design. (e) The prototype of Fe-Arm. (f) Embedded foam design and geometrical parameters. L_{gap} is the length of the gap between levels. L_{ic} is the length of the initial compression. L_i is the initial length of the foam.

vertebraic joint design [7] is proposed to enhance payload and stiffness. [8] and [9] employ particle jamming and embedded Shape Memory Alloy springs, respectively, to achieve variable stiffness. However, the influences of the designs on the oscillations issue have yet to be systematically investigated.

Foams have emerged as a novel material in soft robot fabrication, offering diverse benefits. Poroelastic foam has been utilized for the simple fabrication of soft robots [10]. Additionally, polyethylene foam has enabled the construction of human-scale soft robots [11]. Researchers have successfully employed polyurethane foam in the creation of soft grippers and even soft robotic "puppies" [12]. In the context of pneumatic actuators, polyurethane foam material has been ingeniously incorporated into vacuum-powered designs by brushing a silicone layer onto the surface of the foam [13]. This modularized design enabled soft robots with expanded capabilities and achieved a lightweight structure with variable density and high deformation tolerance. Memory foam, a specific type of polyurethane foam, possesses viscoelastic properties and low-resilience characteristics [14], [15], making it highly suitable for structural support and oscillations reduction of soft robotic arms. In the domain of inverse kinematic modeling for soft robotic joints and arms, due to fabrication errors and the complex dynamics inherent in soft systems, traditional analytical models face challenges in accurately mapping sensor readings to system states [16]. For instance, the widely used Piecewise Constant-curvature method encounters difficulties in this regard [17]. To address these challenges, recent studies have explored the application of various machine learning techniques, with a particular focus on deep learning methodologies [18], [19], [20]. Deep learning-based methods have been extensively studied in the field of inverse kinematic modeling and control of soft pneumatics bellows-based robot arms. Various models such as fully connected networks (FCNs), recurrent neural networks (RNNs), and Convolutional Neural Networks (CNNs) have demonstrated high performance in static modeling of soft arms [21].

However, two-fold major challenges are faced if using existing methods directly. Firstly, previous work on inverse kinematic (IK) modeling mostly does not involve additional components with different material properties such as foam [22], [23], which exerts a force of different directions at the same endpoint position, determining if the foam is being elongated or compressed, as shown in Fig. 1(a). Secondly, when employing deep learning techniques for modeling soft robotic arms, a substantial challenge revolves around acquiring an adequate volume of high-quality labeled training data [20].

In this letter, we present solutions to address the oscillation problem in soft robotic arms through the design of joints and the challenges in modeling and control. Our proposed approach involves a foam-embedded soft robotic joint, which mitigates undesired oscillations. This joint design is seamlessly integrated into a new continuum soft robotic arm, resulting in improved mechanical motion performance while maintaining inherent compliance and flexibility. To achieve cost-effective control, we employ an LSTM-based iterative self-improving learning method for modeling the arm. An origin is explicitly defined as the start point of each model sequence, to enable our RNN model to compress omnidirectional motion information owning to the deformation of the embedded foam. We demonstrate the effectiveness of this approach through real motion control experiments. The contributions of this work can be summarized as follows:

- Introduced a novel foam-embedded soft robotic joint design (Fe-Joint) that effectively reduces undesired oscillations in soft robotic motion, obtaining the quasi-static behavior for inverse kinematic modeling.
- Integrated the Fe-Joint into the new continuum soft robotic arm (Fe-Arm), and defined four key performance metrics to optimize the design further. Realized pneumatic-based active motion control of the Fe-Arm in three degrees of freedom (DOFs).

TABLE I
GEOMETRICAL CONFIGURATIONS OF THE FE-ARM

Parameter	Value(unit)
The initial height	240mm
The maximum extension length	255mm
The minimum contraction length	115mm
The maximum radius of cross-section	70mm
The horizontal distance between the two bellows' axis	69.28mm
The maximum diameter of the bellows	37.56mm
The minimum diameter of the bellows	30.94mm

Fig. 2.   Schematic diagram of passive evaluation experiment.

- Proposed an iterative self-improving learning strategy (ISL) with the LSTM architecture for end-to-end inverse kinematic modeling of the Fe-Arm. Investigated the effect of two control parameters (delay time and step size) on the modeling approach. Achieved a modeling error of less than 9% relative to the maximum horizontal radius of motion, even with limited data availability and human intervention. The generalization potential of the method is demonstrated.

II. DESIGN AND OPTIMIZATION

A. Foam-Embedded Design and Fabrication

As shown in Fig. 1(c), the Fe-Joint is developed by combining distinct dynamic properties of foam and bellows. The active actuation component leverages the high scalability of pneumatic bellows. Blow-molded pneumatic bellows with open ends are employed, concatenating together with 3D-printed nylon planes. To ensure airtightness, we seal the bellows using the hot-melt adhesive (HMA). The passive energy absorption component capitalizes on the viscoelasticity and low resilience of the foam. Each foam is cropped to fit within the space between the bellows, serving as the core element of absorbing elastic potential generated by the bellows during motion.

As illustrated in Fig. 1(d) and (e), the Fe-Arm is constructed by connecting four Fe-Joints in series. To reduce the overall system's DOF and mitigate buckling, 3D-printed connectors are used to link each joint and constraint. All bellows actuators in one vertical line are connected internally and share the same pneumatic pressure. This design enables the Fe-Arm to actuate with three independent pressure inputs, resulting in three actuated DOFs. To facilitate the insertion of foam into the Fe-Arm, the foams are cut into specific shapes, as depicted in Fig. 1(d). In contrast to the integrated design driven by negative pressure presented in [13], our design aims to separate the foam from the actuators, with the foam embedded in parallel to the actuators, and obtain extension and retraction when subjected to positive and negative pressures, respectively. This enables easy replacement of the foam, allowing for a variety of foam configurations to be used with the same soft arm for desired performance. Additionally, nylon belts are employed to secure the assembled parallel structure at each joint, ensuring the desired curvature shape during movements. Geometrical configurations of the Fe-Arm are shown in Table I.
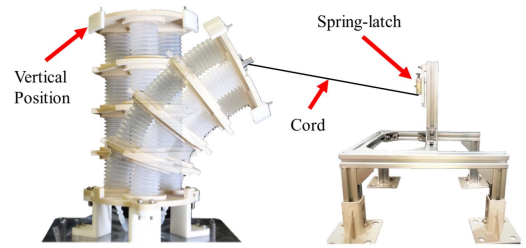
B. Performance Evaluation

To conduct a comparative analysis of different foam-embedded designs and assess their performance, a passive evaluation experiment is employed. As shown in Fig. 2, the unloaded Fe-Arm is subjected to a passive evaluation experiment setup. A thin inelastic soft cord is attached to the end plate of the Fe-Arm and fixed to a point in space. Upon releasing the cord, the Fe-Arm exhibits an immediate tendency to restore its original vertical state. This behavior is attributed to the internal actuation force resulting from the pressure difference between the actuators' cavities and the reaction force arising from structural deformation. To capture and analyze the Fe-Arm's motion, an inertial measurement unit (MPU-6050) is mounted on the end plate. This allows for the recording of pitch angle and acceleration data during the motion of the Fe-Arm.

To compare different foam-embedded designs in the passive evaluation experiment, we propose four metrics to assess their performance: (a) a_{peak}: The peak acceleration experienced by the end plate of the Fe-Arm. (b) T_{stable}: The relative stability time is defined as the duration required for the Fe-Arm to reach the quasi-static state. It is determined by identifying the time instant when the third peak of the pitch angle is reached. (c) $T_{settling}$: The settling time is defined as the duration it takes for the acceleration of the Fe-Arm to reduce to a range between 0.85 g and 1.05 g, which corresponds to a 5% error relative to the steady-state acceleration. (d) Δ_{angle}: This metric quantifies the angular difference between the final state of the Fe-Arm and its initial vertical state after stabilization.

C. Configuration Iteration

We conducted experiments to achieve the best foam-embedded design, focusing on three key aspects. Firstly, we compare two different materials, high-resilience foam and memory foam, with no foam to evaluate the impact of foam material on the arm's performance. Next, we explored the influence of foam density by testing three different density levels. Lastly, we investigated the effect of two geometrical parameters: the length of the gap between levels (L_{gap}) and the length of the initial compression (L_{ic}), as shown in Fig. 1(d). L_{gap} brings more flexibility for the foam between levels of the joints. With larger L_{ic}, the actuators can extend easier with less constraint from the foam due to the easy-to-compressed and hard-to-elongated characteristics of the foam. For each of these optimization aspects, we performed the passive evaluation experiment and utilized the
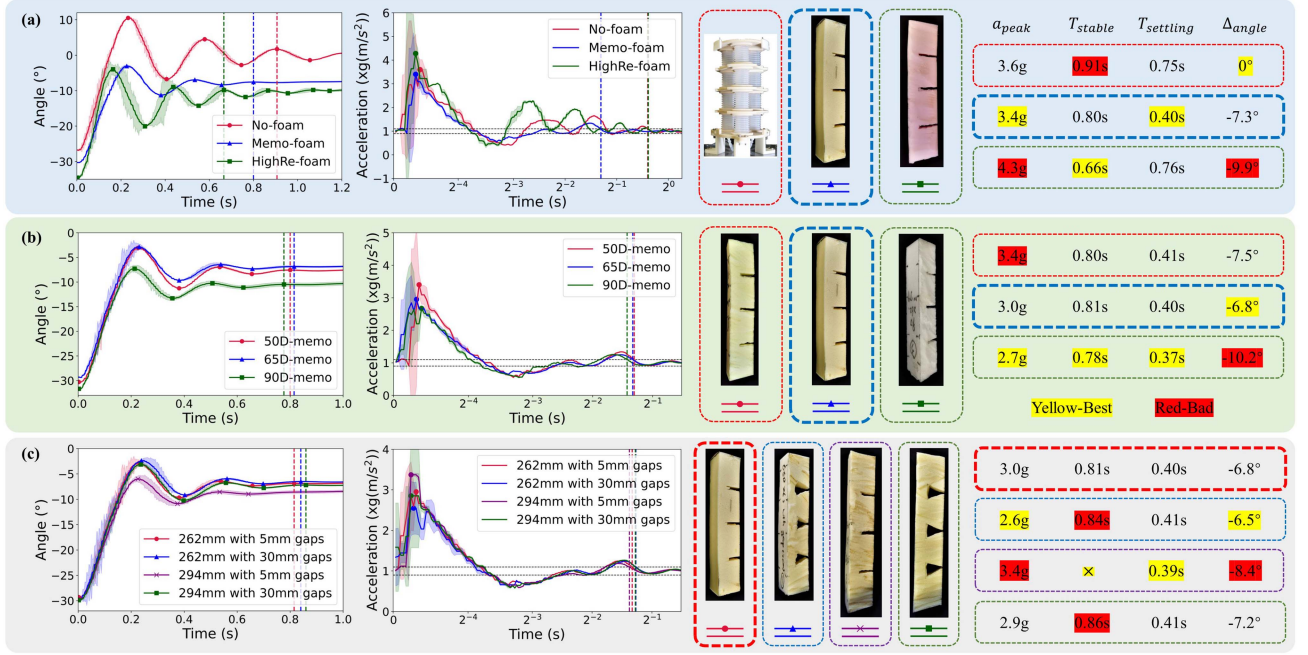
Fig. 3. Passive evaluation experiment results. From left to right are, respectively, angular and acceleration graphs, physical photos of the design used, and values of four metrics. a_{peak}: peak dots in the acceleration graphs; T_{stable}: dashed lines in the angle graphs; $T_{settling}$: dashed lines in the acceleration graphs; Δ_{angle}: values of the end of curves in the angle graphs. Distinct designs are represented by varying colors of curves and dashed edges. The chosen designs are accentuated with thickened dashed edges. (a) Material comparison. (b) Density comparison. (c) Geometrical parameters comparison.

metrics mentioned to evaluate and compare the performance of the optimized designs.

The passive evaluation experiment results are shown in Fig. 3. In the comparison experiment of different foam materials, memory foam stands out by manifesting a significant reduction in a_{peak} of 3.4 g and $T_{settling}$ of 0.4 s, compared to the other two designs. Although the T_{stable} of 0.8 s is longer than that of the high-resilience foam (0.66 s), the latter exhibits more oscillations in subsequent movements and a large Δ_{angle} of $-9.9°$. These observations underscore that memory foam is a suitable choice for mitigating oscillations and improving performance, a result attributed to its superior viscoelastic and low-resilience characteristics.

To investigate the impact of foam density, we conducted comparison tests using different densities of memory foam: 50D, 65D, and 90D. The results show that the 65D memory foam exhibits similar performance to the 50D memory foam in terms of T_{stable} of 0.81 s and $T_{settling}$ of 0.4 s. However, it significantly outperforms the 50D memory foam in a_{peak} with a value of 3 g. On the other hand, the 90D memory foam demonstrates a large Δ_{angle} of $-10.2°$. Consequently, the 65D memory foam is considered to be the better choice in terms of foam density.

The geometrical design parameters were optimized using 65D memory foam. Tests compared 262 mm and 294 mm values for L_i (equivalent to 28 mm and 60 mm L_{ic}), 5 mm and 30 mm values for L_{gap}. It was observed that the designs with 5 mm gaps exhibited excellent performance in terms of T_{stable} and $T_{settling}$ compared to the 30 mm one. However, the 294 mm design with 5 mm gaps showed a relatively large Δ_{angle} of $-8.4°$, and the difference in a_{peak} between the 262 mm design with 30 mm

and 5 mm gaps was not substantial. Overall, the configuration with 262 mm L_i and 5 mm L_{gap} yielded the relatively best performance among the tested designs. Therefore, the 262 mm L_i and 5 mm L_{gap} 65D memory foam was chosen for further research, and the modeling of the Fe-Arm was implemented based on this configuration.

D. Sensing and Motion Control

The end position of the Fe-Arm is measured using the Orbbec Astra Mini monocular RGB depth camera, as shown in Fig. 4(a). This process involves identifying the blue sticker on the end plate and extracting the center point's coordinates from the point cloud data. The pneumatic actuation module consists of the micro-controller unit (MCU), solenoid valves, pressure sensors, and other parts, as shown in Fig. 4(b). Fig. 4(c) compares forward direction actuation pressure with and without enhancement of foam, and shows that impact of the foam on the driving power can be disregarded. The STM32F103C8T6 is used as the MCU to control the whole system. The air pressure sensors are connected in series with the output air circuit to measure the three actuation pressures of the Fe-Arm respectively.

Using pneumatic control without any feedback, the Fe-Arm is capable of executing simple movements within its workspace with manual control inputs. The trajectories of the Fe-Arm in the vertical, side, and forward three DOFs, along with the corresponding actuation pressure values, are depicted in Fig. 4(d) and (e), respectively. Specifically, the Fe-Arm can achieve a lateral 90° bend, a longitudinal contraction of 125 mm, and an extension of 15 mm relative to its initial length, as demonstrated in Fig. 4(f).
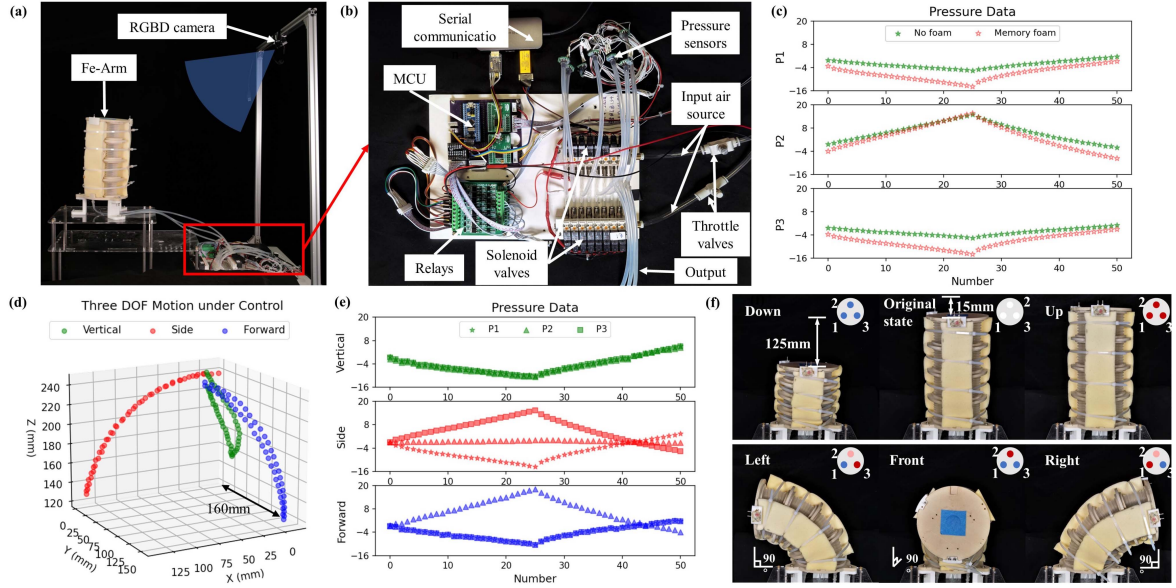
Fig. 4. (a) End position detection module. (b) Pressure measurement and control module. (c) Forward direction actuation pressure with and without enhancement of foam shows that embedded foam will not significantly increase the burden of the actuation system. (d) Motion trajectories of three DOFs. (e) Actuation pressure values of motion in three DOFs. (f) Mechanical performance demonstration of the Fe-Arm. Blue indicates deflate, red indicates inflate, and white indicates atmospheric pressure. Color shades correspond to bellows' internal pressure level.

The maximum horizontal radius of motion is 160 mm, as shown in Fig. 4(d).

III. ITERATIVE SELF-IMPROVING LEARNING FOR END-TO-END INVERSE KINEMATIC MODELING

A. Modeling Method Architecture

Due to the foam-embedded structure of the Fe-Arm, the material property of memory foam has the capacity to store motion potential energy and subsequently release it slowly. As a result, the present state of the Fe-Arm is notably influenced by its preceding state during continuous movement. This dynamic gives rise to an intractable scenario where a specific set of pressure values within the actuation space may correspond to multiple distinct end positions in the task space, depending on the entire trajectory the arm traveled from.

To effectively capture and respond to the intricate relationship between the sequence of antecedent states and the current state of the Fe-Arm, we employ RNNs for data-driven end-to-end inverse kinematic modeling. Specifically, we utilize the LSTM model [24] to address this particular challenge. The inputs and outputs are illustrated below:

$$p(k) = f^{-1}(p(0), p(1), \ldots, p(k-1), t(k)), \qquad (1)$$

where the input pressure values of the actuators at the moment k are represented by $p(k)$, denoting the actuation space; the corresponding target space end position of the Fe-Arm is denoted by $t(k)$. Specifically, we fix $p(0)$ and $t(0)$ to guarantee the repeatability of the trained model.

To address the demand for high-quality training data, we propose an iterative self-improving learning (ISL) strategy designed to model for a specific target trajectory using a limited dataset.

The agent starts with a limited amount of labeled data. Then the agent uses the available labeled data to make predictions, which are then applied to the Fe-Arm. This results in obtaining real actuation pressure and end position data. However, due to the scarcity of high-quality data, the actual motion trajectories exhibit significant deviations from the target trajectories. These real motion data are then reintroduced into the training set for continuous iteration. Through iterative training on this combined set of labeled and low-quality data, the proposed learning strategy effectively generates more training samples and improves the model's performance with minimal human intervention. The overall modeling method procedure is illustrated in Fig. 5, with the red section depicting the process of the ISL. The four trajectory plots correspond to the tracking results of the quadrilateral-shaped trajectory in four iterative trainings, respectively.

B. Data Acquisition

Due to the symmetry of the Fe-Arm structure, our investigation is focused on the forward 120° workspace, as shown by the light green region in Fig. 6(a), for the sake of simplicity. The modeling method can be extended to the entire workspace.

As an initial model needs to be obtained before the self-improving iterations, we also collect a simple initial training set. The initial training set contains four sets of the simplest and easiest to control trajectories, which are the forward, both sides of the 60° vertical plane, and the vertical direction. Each set of data is a downward motion from the original vertical state and then returns upward, as shown in Fig. 6(a). The Fe-Arm was first fixed at the original vertical position using external support structures to ensure consistency for each experiment.
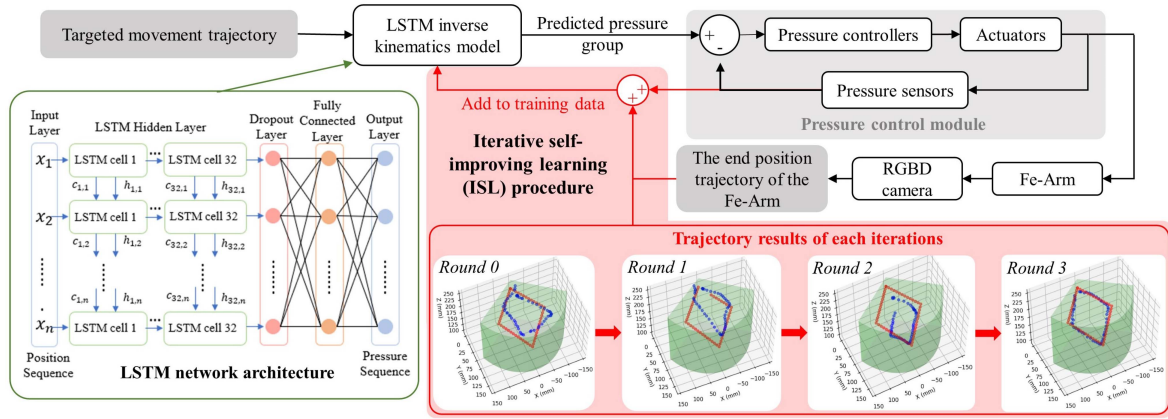
Fig. 5. Schematic diagram of the LSTM-based iterative self-improving learning method (ISL) for end-to-end inverse kinematic modeling.
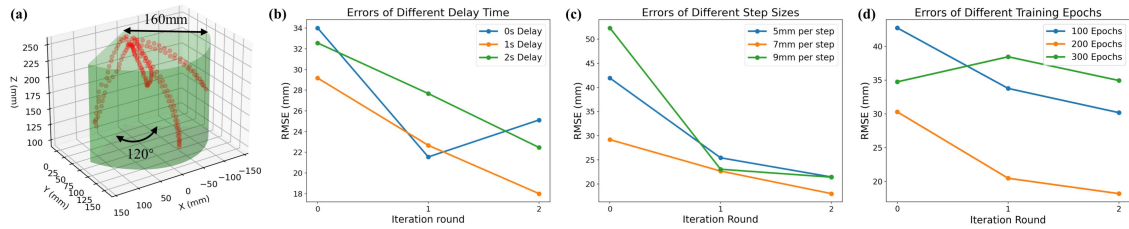

Fig. 6. (a) Initial training set and focused workspace. (b) The effects of different delay times on modeling. (c) The effects of different step sizes on modeling. (d) The effects of different epochs on modeling.

Then remove the supports and start actuating. Each completed actuation immediately reads the three pressure values at that time. After waiting for several seconds, the Fe-Arm reaches quasi-static, and the camera takes a photo and measures the coordinates of the end position at this point. The complete data set contains the three actuation pressures and the 3D position coordinates of all data points. All data acquisition and testing are performed according to this process.

C. Control Parameters Optimization

Two parameters that influence the inverse kinematics modeling during the control process are (a). the time delay required to attain quasi-stasis after each step (T_{delay}) and (b). the distance between each incremental movement step (L_{step}). Considering the Fe-Arm need to ensure quasi-static conditions during inverse kinematics modeling, the memory foam's slow rebound property requires a delay time after each actuation. A brief delay can prevent the Fe-Arm from reaching quasi-static, while a prolonged delay could disrupt motion continuity. A larger step size results in a smaller sampling frequency, while a smaller step size can introduce higher randomness fluctuations due to systematic errors. Therefore, finding the right balance between these two parameters is crucial to achieving accurate and stable inverse kinematics modeling while ensuring smooth and continuous robot motion.

We conducted two rounds of iterations using the same target trajectory (lower quadrilateral, as shown in Fig. 7(a)), comparing

the effects of different delay times (0 s, 1 s, 2 s) and step sizes (5 mm, 7 mm, 9 mm) on modeling accuracy. The results are depicted in Fig. 6(b) and (c). Notably, optimal modeling performance was consistently achieved with the middle values of T_{delay} and L_{step}, specifically 1 s delay and 7 mm per step. These values yielded the least error across multiple rounds. In round 2, errors reached a minimum of 18.00 mm and 21.45 mm, respectively. The corresponding percentage errors relative to the maximum horizontal radius of motion are 11.25% and 13.4%. Both parameter values demonstrated improvement trends during iterations. As a result, these two values are chosen as the control parameters for subsequent modeling tasks. The anomalies observed in the case of a 0 s delay situation can be attributed to the inherent instability and oscillations. Inadequate time for the Fe-Arm to reach a quasi-static state, led to increased random errors, resulting in modeling errors that did not consistently decrease, along with the occurrence of unusual volatility.

D. Neural Network Design and Training

PyTorch is used for building models, training, and inference. The specific LSTM-based model architecture we use is shown in Fig. 5. The network commences with a sequential input layer, incorporating three dimensions (3D) of end position coordinates, relative to the coordinate system anchored at the base of the Fe-Arm. It is followed by two LSTM hidden layers, each comprising 32 hidden neurons. To prevent overfitting and to make
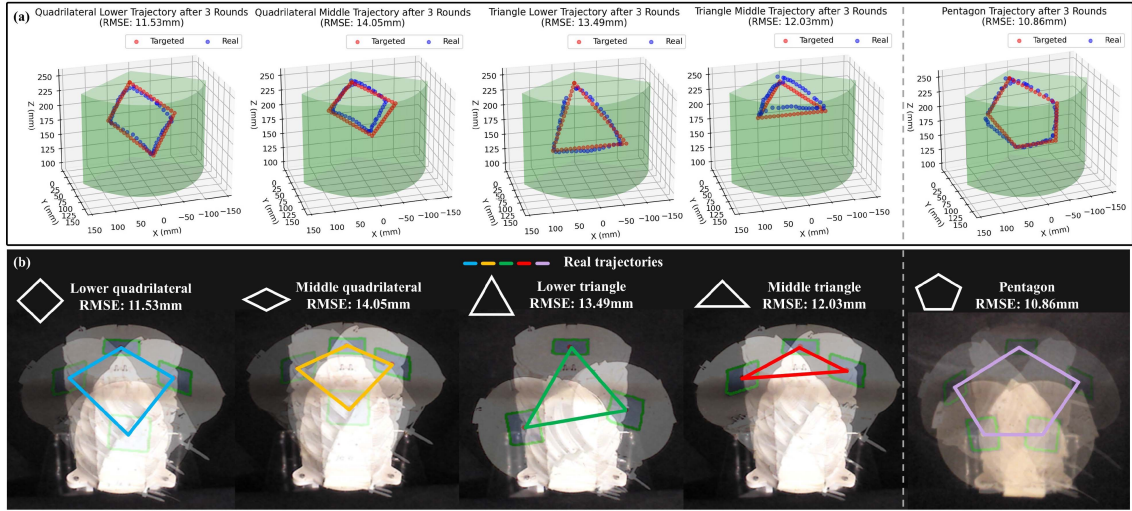
Fig. 7. Modeling results of trajectories after three round iterations. The left side of the dotted line is the training trajectory and the right side is the validation pentagonal trajectory. (a) The 3D position comparison between the target trajectories and the real trajectories. (b) Photos of motion trajectories shot by RGBD camera.

the prediction and modeling more robust to noise, a dropout layer is added after the LSTM layer, with a dropout rate of 0.2. This is followed by a fully connected linear mapping layer of the same size for mapping the position to the pressure. Finally, the output layer produces the three internal actuation pressure values. The training process utilizes the adaptive moment estimation (Adam) algorithm to expedite convergence and efficacy. The mean squared error loss function (RMSE) is used as the loss function.

To determine the value of the training epoch of the model, we also conducted two rounds of iterations to compare the performance of models trained with three different numbers of epochs. The results are depicted in Fig. 6(d), indicating that 100 epochs resulted in lower modeling accuracy. Conversely, employing 300 epochs led to overfitting, as the errors did not exhibit a decreasing trend. Thus, we determined that the optimal number of training epochs for our model is 200.

E. Modeling Results

We designed four different movement trajectories for training, consisting of two different sizes of quadrilaterals and triangles, as shown in Fig. 7. We employed the ISL strategy outlined above to train a unified model using data collected from all four trajectories, in both clockwise and counterclockwise directions. Fig. 7(a) and (b) illustrate the trajectory outcomes in 3D space and through real images, after three rounds of self-improving iterations, respectively. The RMSEs of the real trajectories controlled with predicted pressure compared to the target trajectories are presented in Fig. 8(a). Additionally, the corresponding percentage errors relative to the maximum horizontal radius of motion are summarized in Table II. Across three round iterations, the RMSEs for all four motion trajectories remained below 15 mm, with relative errors consistently within 9%. Notably, the smallest modeling error after three iterations was observed
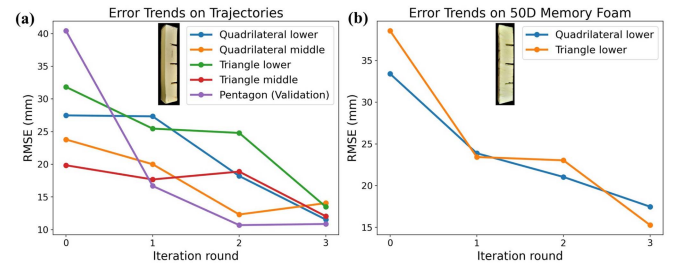

Fig. 8. RMSEs of real trajectories vs. target trajectories for (a) 65D memory Fe-Arm and (b) 50D memory Fe-Arm.

TABLE II
RELATIVE ERRORS OF TRAJECTORIES W.R.T. THE MAXIMUM HORIZONTAL RADIUS OF MOTION

Trajectories	Round 0	Round 1	Round 2	Round 3
Lower Quadrilateral	17.17%	17.08%	11.37%	**7.20**%
Middle Quadrilateral	14.86%	12.50%	**7.69**%	8.78%
Lower Triangle	19.89%	15.91%	15.49%	**8.42**%
Middle Triangle	12.40%	11.04%	11.79%	**7.52**%
Pentagon	25.26%	10.42%	**6.67**%	6.78%

The bold values are to highlight best results regarding each experiment.

in the lower quadrilateral, measuring 11.53 mm and 7.20%. Furthermore, to validate whether the result was prone to overfitting on training trajectories, we introduced an additional pentagon validation trajectory that was not included in any training or learning process. After only two iteration rounds, the pentagon test trajectory exhibited the smallest error, with an RMSE of 10.68 mm and a relative error of 6.67%. The result remained almost consistent after three rounds. This outcome underscores the robustness of the ISL method on different trajectories.

The proposed ISL strategy for end-to-end inverse kinematics modeling of the Fe-Arm enhances prediction accuracy as iterations progress. Particularly noteworthy is the observed reduction

of the quadrilateral middle error to 12.31 mm in the second iteration, which implies that modeling errors tend to stabilize and converge with an increase in iterations due to control and system factors. The actual control mean absolute deviation (MAD) of the pressure feedback control process for the target actuation pressure per way is 0.33 kPa. Due to this system control error, the true accuracy of this modeling technique is anticipated to surpass the reported outcomes.

Furthermore, to show the adaptability of the proposed ISL method, we used the predicted pressure control sets obtained from round three and applied them to the Fe-Arm featuring 262 mm L_i and 5 mm L_{gap} with 50D memory foam. Subsequently, we utilized the newly acquired real-world data from the execution of quadrilateral and triangle trajectories as our training set to continually iterate and construct a new model for the 50D memory Fe-Arm. Despite the suboptimal foam material and the limited data, the modeling results demonstrated a decrease in error, with RMSEs of 17.47 mm and 15.26 mm for quadrilateral and triangle trajectories, as shown in Fig. 8(b). In summary, the collective findings illustrate that this ISL modeling approach attains superior accuracy even with a limited number of iterations and a constrained dataset of high quality. The performance also underscores the methodology's portability and adaptability across various configurations.

IV. CONCLUSION

This letter focused on the issues of soft robot arm oscillation and instability during control. Leveraging memory foam's unique viscoelastic and low-resilience characteristics, we have successfully engineered a Fe-Joint design that reduces oscillations during motion. This design has been incorporated into the Fe-Arm with an iterative optimization process refining design configurations. The resultant mechanical performance of the Fe-Arm showcases exceptional control potential across stability and an expansive workspace while retaining its inherent flexibility and compliance.

With the appropriate foam components, the movements of the Fe-Arm can be considered quasi-static and are able to be controlled by inverse kinematic modeling. An LSTM-based iterative self-improving end-to-end inverse kinematics modeling method is hence proposed, specifically tailored to the Fe-Arm's mechanical intricacies. Through the optimization of control parameters, the methodology achieved trajectory modeling errors consistently less than 16 mm and a mere 10% with respect to the workspace radius. The best modeling result, after three rounds of iterations, reached an error of 12.26 mm and 7.67%. These results were achieved while working with restricted datasets, iteration cycles, and limited human intervention. Furthermore, our proposed learning strategy enhanced model prediction accuracy through the iterative process, exemplifying its efficacy in ensuring precise trajectory tracking under open-loop control paradigms. Finally, we demonstrated the generalization potential of the ISL method using a pentagonal trajectory and on a Fe-Arm configuration with different foam components.

In future work, it is worth exploring the optimal configuration of foam structure through the dynamic model of the arm as a mass-spring-damper system for enhancing performance. Also, to further validate the proposed ISL method, it is also worthwhile to apply it to other soft arm structures.

REFERENCES

[1] D. Rus and M. T. Tolley, "Design, fabrication and control of soft robots," *Nature*, vol. 521, no. 7553, pp. 467–475, 2015.

[2] R. Kang, Y. Guo, L. Chen, D. T. Branson, and J. S. Dai, "Design of a pneumatic muscle based continuum robot with embedded tendons," *IEEE/ASME Trans. Mechatron.*, vol. 22, no. 2, pp. 751–761, Apr. 2017.

[3] P. Qi, C. Qiu, H. Liu, J. S. Dai, L. D. Seneviratne, and K. Althoefer, "A novel continuum manipulator design using serially connected double-layer planar springs," *IEEE/ASME Trans. Mechatron.*, vol. 21, no. 3, pp. 1281–1292, Jun. 2016.

[4] S. Yang et al., "Dynamic capture using a traplike soft gripper with stiffness anisotropy," *IEEE/ASME Trans. Mechatron.*, vol. 28, no. 3, pp. 1337–1346, Jun. 2023.

[5] V. Falkenhahn, A. Hildebrandt, R. Neumann, and O. Sawodny, "Dynamic control of the bionic handling assistant," *IEEE/ASME Trans. Mechatron.*, vol. 22, no. 1, pp. 6–17, Feb. 2017.

[6] A. D. Marchese and D. Rus, "Design, kinematics, and control of a soft spatial fluidic elastomer manipulator," *Int. J. Robot. Res.*, vol. 35, no. 7, pp. 840–869, 2016.

[7] J. Liu, X. Wang, S. Liu, J. Yi, X. Wang, and Z. Wang, "Vertebraic soft robotic joint design with twisting and antagonism," *IEEE Robot. Automat. Lett.*, vol. 7, no. 2, pp. 658–665, Apr. 2022.

[8] C. Yang et al., "Geometric constraint-based modeling and analysis of a novel continuum robot with shape memory alloy initiated variable stiffness," *Int. J. Robot. Res.*, vol. 39, no. 14, pp. 1620–1634, 2020.

[9] Y. Li, T. Ren, Y. Chen, and M. Z. Chen, "A variable stiffness soft continuum robot based on pre-charged air, particle jamming, and origami," in *Proc. IEEE Int. Conf. Robot. Automat.*, 2020, pp. 5869–5875.

[10] B. C. M. Murray et al., "Poroelastic foams for simple fabrication of complex soft robots," *Adv. Mater.*, vol. 27, no. 41, pp. 6334–6340, 2015.

[11] S. Li et al., "Scaling up soft robotics: A meter-scale, modular, and reconfigurable soft robotic system," *Soft Robot.*, vol. 9, no. 2, pp. 324–336, 2022.

[12] L. Somm, D. Hahn, N. Kumar, and S. Coros, "Expanding foam as the material for fabrication, prototyping and experimental assessment of low-cost soft robots with embedded sensing," *IEEE Robot. Automat. Lett.*, vol. 4, no. 2, pp. 761–768, Apr. 2019.

[13] M. A. Robertson and J. Paik, "New soft robots really suck: Vacuum-powered systems empower diverse capabilities," *Sci. Robot.*, vol. 2, no. 9, 2017, Art. no. eaan6357.

[14] A. Sfaoui, "On the viscoelasticity of the polyurethane foam," *J. Acoustical Soc. Amer.*, vol. 97, no. 2, pp. 1046–1052, 1995.

[15] M. A. Garrido, R. Font, and J. A. Conesa, "Kinetic study and thermal decomposition behavior of viscoelastic memory foam," *Energy Convers. Manage.*, vol. 119, pp. 327–337, 2016.

[16] D. Gan, J. S. Dai, J. Dias, and L. Seneviratne, "Reconfigurability and unified kinematics modeling of a 3rTPS metamorphic parallel mechanism with perpendicular constraint screws," *Robot. Comput.- Integr. Manuf.*, vol. 29, no. 4, pp. 121–128, 2013.

[17] R. J. Webster III and B. A. Jones, "Design and kinematic modeling of constant curvature continuum robots: A review," *Int. J. Robot. Res.*, vol. 29, no. 13, pp. 1661–1683, 2010.

[18] K. Chin, T. Hellebrekers, and C. Majidi, "Machine learning for soft robotic sensing and control," *Adv. Intell. Syst.*, vol. 2, no. 6, 2020, Art. no. 1900171.

[19] X. Wang, Y. Li, and K.-W. Kwok, "A survey for machine learning-based control of continuum robots," *Front. Robot. AI*, vol. 280, 2021, Art. no. 730330.

[20] D. Kim et al., "Review of machine learning methods in soft robotics," *Plos One*, vol. 16, no. 2, 2021, Art. no. e0246102.

[21] L. Wang et al., "Soft robot proprioception using unified soft body encoding and recurrent neural network," *Soft Robot.*, vol. 10, pp. 825–837, 2023.

[22] Y. Ansari, M. Manti, E. Falotico, M. Cianchetti, and C. Laschi, "Multiobjective optimization for stiffness and position control in a soft robot arm module," *IEEE Robot. Automat. Lett.*, vol. 3, no. 1, pp. 108–115, Jan. 2018.

[23] T. G. Thuruthel, E. Falotico, F. Renda, and C. Laschi, "Model-based reinforcement learning for closed-loop dynamic control of soft robotic manipulators," *IEEE Trans. Robot.*, vol. 35, no. 1, pp. 124–134, Feb. 2019.

[24] S. Hochreiter and J. Schmidhuber, "Long short-term memory," *Neural Computation*, vol. 9, no. 8, pp. 1735–1780, 1997.